ARTICLE

doi:10.1038/nature11057

Brain-wide neuronal dynamics during motor adaptation in zebrafish

Misha B. Ahrens[1,2], Jennifer M. Li[1], Michael B. Orger[3], Drew N. Robson[1], Alexander F. Schier[1], Florian Engert[1] & Ruben Portugues[1]

A fundamental question in neuroscience is how entire neural circuits generate behaviour and adapt it to changes in sensory feedback. Here we use two-photon calcium imaging to record the activity of large populations of neurons at the cellular level, throughout the brain of larval zebrafish expressing a genetically encoded calcium sensor, while the paralysed animals interact fictively with a virtual environment and rapidly adapt their motor output to changes in visual feedback. We decompose the network dynamics involved in adaptive locomotion into four types of neuronal response properties, and provide anatomical maps of the corresponding sites. A subset of these signals occurred during behavioural adjustments and are candidates for the functional elements that drive motor learning. Lesions to the inferior olive indicate a specific functional role for olivocerebellar circuitry in adaptive locomotion. This study enables the analysis of brain-wide dynamics at single-cell resolution during behaviour.

The generation of motor output and the influence of sensory input on future motor programs engage neural activity in many neurons across multiple brain regions. However, past measurements of neural activity during behaviour have been hampered by the inability to monitor exhaustively all neurons in the brain of a behaving animal. Although it is possible to record activity from behaving animals[1–6], the large size and opacity of the vertebrate brain constrains experimenters to focus on small fractions of the total number of neurons. Here we develop a preparation in which neuronal activity can be monitored anywhere in the brain using two-photon calcium imaging in paralysed larval zebrafish that interact with a virtual environment and adjust their behaviour to changes in visual feedback.

When visual feedback following a motor command does not meet expectation, animals can learn to adapt the strength of subsequent motor commands. In the past this has been studied in controlled laboratory settings by perturbing visual feedback in the context of insect flight[7–9], the vestibulo-ocular reflex[10,11] and reaching movements[12,13]. Here we study adaptive control of locomotion in larval zebrafish[14]. This animal swims in discrete swim bouts during which the visual environment moves relative to its retina. One hypothesis is that this optic flow is used as a measure of displacement and serves to tune the strength of future motor commands to the desired travel distance[7–9]. Such sensorimotor recalibration is particularly important during the optomotor response[15,16], in which animals move in the direction of motion of the visual surround—thereby stabilizing their location in the presence of, for example, water flow—a response that occurs in many animal species. If motor output is not correctly calibrated to visual feedback, a fish may systematically overshoot or undershoot the desired travel distance, instead of stabilizing its location. Sensorimotor recalibration is necessary for accurate locomotion because the rate of optic flow following a motor command is affected by temperature-dependent changes in muscle strength, the viscosity of the water and the distance of objects from the retina.

To examine neural dynamics across brain areas that drive sensorimotor recalibration, we developed a system to study neural activity at cellular resolution[17,18], using two-photon microscopy[19], anywhere in the brain[20] during closed-loop optomotor behaviour in larval zebrafish. These animals have a small and transparent brain that is readily accessible for optogenetic recording and stimulation[21,22], electrophysiology[23] and single-cell ablation[24]. To remove motion artefacts[25,26], we developed a swim simulator for completely paralysed larvae (Fig. 1a). Motor commands, or 'fictive swims', are recorded at the motor neuron level[8,27,28] (Fig. 1c, d) and translated, in real time, into visual feedback that resembles the optic flow of freely swimming fish (Methods). This constitutes a fictively driven virtual-reality setup. Simultaneously, a two-photon microscope scanning over a transgenic fish expressing GCaMP2 (ref. 29) in almost all neurons[20,30] allows activity to be monitored throughout the brain at single-neuron resolution. As the experimenter is in complete control of the visual feedback, this allowed us to study neural dynamics during visually guided motor adaptation throughout the brain at the cellular level.

Fictive motor adaptation

To study motor adaptation, we used a closed-loop paradigm and simulated a one-dimensional environment in which the fish is swept backwards by a virtual water flow, a motion that the fish was able to compensate for by swimming forwards, as in the optomotor response. In the fictive virtual-reality setup, this corresponds to a whole-field visual stimulus that is moving forwards but that can be momentarily accelerated backwards by a fictive swim of the fish (Fig. 1b; Methods), so that the fish can stabilize its virtual location over time. Remarkably, paralysed larval zebrafish behaved readily in this closed-loop paradigm, showing similar behaviour to freely swimming fish that are exposed to whole-field motion[24], and were not noticeably compromised by the absence of vestibular, proprioceptive and somatosensory feedback that accompanies unrestrained swimming.

An important free parameter in this closed-loop paradigm is the feedback gain[10,11,12,14,31]— the factor that translates the strength of the fictive swim signal to the change in stimulus velocity (Methods). The higher the feedback gain, the greater the velocity change following a motor command (for example, dashed red line in Fig. 1b), so that high feedback gain corresponds to a 'strong virtual fish' and low feedback

[1]Department of Molecular and Cellular Biology, Harvard University, 16 Divinity Avenue, Cambridge, Massachusetts 02138, USA. [2]Computational and Biological Learning Laboratory, Department of Engineering, Cambridge University, Trumpington Street, Cambridge CB2 1PZ, UK. [3]Champalimaud Neuroscience Programme, Champalimaud Centre for the Unknown, Avenida Brasília, Doca de Pedrouços, 1400-038 Lisboa, Portugal.

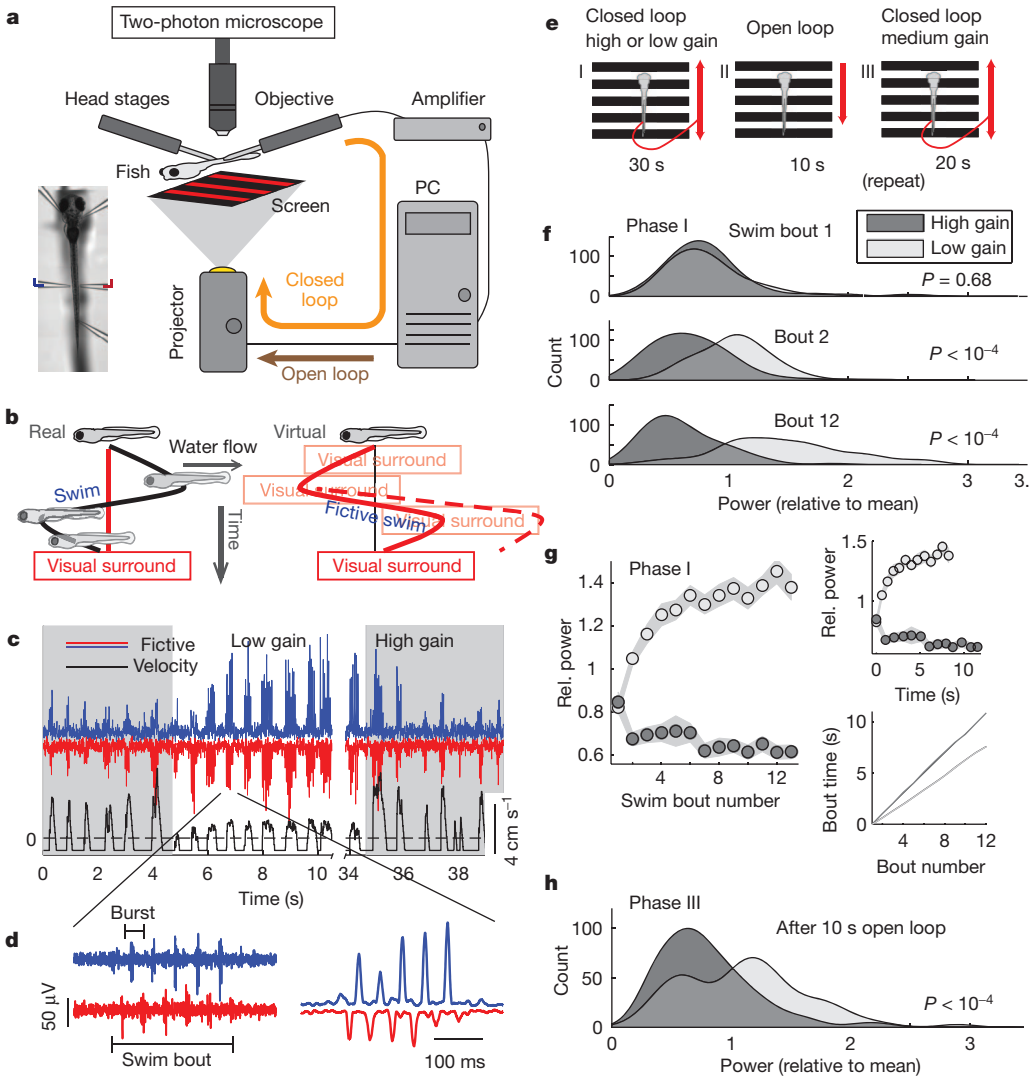

Figure 1 | Experimental setup and fictive motor adaptation. **a**, Schematic of the setup. Photograph of a paralysed larval zebrafish (left) in the experimental setup (right), supported by pipettes, two of which are recording pipettes. **b**, Illustration of the virtual motor adaptation assay. Left, trajectory of a fish executing one swim bout against a water current (black trajectory) in the presence of a visual surround (red). Right, simulation of this behaviour in the virtual environment, in which the visual surround is moved and the fish is stationary. The visual surround is accelerated backwards when a fictive swim occurs. The trajectory that would occur if the feedback gain were higher is shown by a dashed red line. **c**, Fictive motor adaptation. Fictive swim vigour (blue and red traces for left and right channels, respectively) and stimulus velocity (black trace) plotted over time. High and low feedback gain epochs are shown in grey and white. **d**, Example fictive swim bout (left) and corresponding processed trace (right). **e**, Assay to probe sensorimotor adaptation and motor memory formation (left panel, phase I; middle panel, phase II; right panel, phase III). **f**, Power per swim (the area under the processed fictive signal) as a function of swim bout number during adaptation phase I ($n = 5$ fish). **g**, Average power as a function of swim bout number during phase I. Top right, relative swim bout power as a function of time. Bottom right, average time of swim bouts for low gain (light grey) and high gain (dark grey) conditions. **h**, Histogram of relative power of the first swim bout in phase III after either low gain (light grey) or high gain (dark grey) in phase I. Bout power is significantly higher after a low gain epoch than after a high gain epoch.

gain to a 'weak virtual fish'. Accurate motor control would require the motor output to adapt to the feedback gain. Periodically switching the feedback gain between low and high values in the virtual environment resulted in compensatory changes in motor output: a change to a lower gain resulted in the gradual increase of the amplitude and duration of the fictive swim signals (Fig. 1c and Supplementary Movie 1; a weak fish sends more impulses to the muscles), whereas a switch to a higher gain setting led to an incremental decrease (a strong fish sends fewer impulses to the muscles). This behaviour was tested in more detail in the scheme shown in Fig. 1e, which was repeated up to 50 times per fish. We analysed the power of motor nerve bursts, equivalent to the number of fictive tail oscillations (Fig. 1d), in each of the first 12 swim bouts that occurred during 30 s of motor adaptation to either high or low feedback gain (Fig. 1e, phase I). The first swim bouts following a switch from low to high gain, or from high to low gain, were indistinguishable (t-test, $P > 0.5$; Fig. 1f). This implies that fish do not adjust their motor output once a motor command has been issued, despite the presence of immediate visual feedback. Starting at the second swim bout, the power diverges in the high and low gain conditions ($P < 10^{-4}$). Behavioural adjustment plateaus after about ten bouts, which corresponds to approximately 7–10 s (Fig. 1g; Supplementary Fig. 4).

To determine whether the larvae are learning a new sensorimotor transformation or merely responding to different patterns of visual stimulation during the high- and low-gain periods, fish were exposed to a 10-s 'rest' period (Fig. 1e, phase II) during which constant-velocity backward gratings were shown in open loop, a stimulus that tends to inhibit swimming, followed by a closed-loop 'test' period of medium feedback gain (Fig. 1e, phase III). We found that the strength of the first swim bouts in the 'test' period was determined by the gain

setting during the preceding adaptation session (phase I), which shows that the retention of the increased or decreased locomotor drive outlasts 10 s of fixed optic flow (Fig. 1h and Supplementary Fig. 5). Thus, motor adaptation in larval zebrafish is not merely a response to different patterns of visual stimulation, but instead involves a short-term learned change in the sensorimotor transformation.

Brain-wide functional imaging during behaviour

After verifying that neural activity in the reticulospinal system is modulated by locomotor drive (Supplementary Fig. 6a–f), as suggested by previous studies[24], we next looked for signals relating to adaptive motor control throughout the entire brain (Supplementary Movie 2). We generated a transgenic fish expressing the genetically encoded calcium indicator GCaMP2 (ref. 29) driven by the panneuronal *elavl3* (previously known as HuC) promoter[20,30] (Fig. 2a). We used a paradigm in which 30 s of high gain alternated with 30 s of low gain, without open-loop intermissions. Behavioural variables such as swim frequency, number of bursts and power changed in an analogous manner (Supplementary Fig. 4c). A single *z* plane was imaged for six repetitions of gain switches. The brain volume that can be covered in a single fish depends on the duration of the paradigm and the size of the imaging plane. With relatively short assays (about 2 min) the entire brain of a single fish can be imaged in one experiment. We chose instead to use a longer assay—10 min—to cope with our relatively complicated behavioural paradigm and the low signal-to-noise ratio of GCaMP2. Thus, we sampled on average 20% of each fish's brain and created a composite brain for final analysis.

Data analysis was automated and carried out as follows. Every experiment generated a number of fluorescence movies with associated fictive swim recordings and information about the stimulus. A custom-written signal-identification and signal-localization algorithm extracted fluorescence time series from single neurons or 4 × 4-μm regions of neuropil (Fig. 2c–e; Methods). These fluorescence time series (Fig. 2e) were then related to the stimulus and behavioural traces (Fig. 2f) using the methods described below. Finally, to identify the regions of interest (ROIs) of multiple fish with anatomical loci in a reference brain, all imaged planes were mapped using an image-registration algorithm (Supplementary Movie 3) to a high-resolution reference brain of a 6-days-post-fertilization (d.p.f.) larva. Although small variations existed between brains, the large number of landmarks made reasonable localization between different fish possible (within about 25 μm; Methods).

Measurement of motor-related activity

To search the brain for neural activity related to motor output, we first needed to solve the problem that in closed loop, it is not possible to easily distinguish motor- from visual-related activity, as both are directly linked in this setting. A period of open-loop stimulus presentation was added to the paradigm (Fig. 2e, f; yellow area), during which the stimulus experienced by the animal during a preceding closed-loop period (Fig. 2e; black bar) was repeated. Activity of visually driven neurons during this 'replay' period will resemble the activity of the preceding period, and this is formalized by using the correlation coefficient of fluorescence (CCFF) during and before replay, as a measure of the degree of visually driven activity. On the other hand, activity of motor-related neurons will instead correlate to motor output, and this is formalized by CCFM, the correlation coefficient between motor output and fluorescence during replay, as a measure of motor-related activity (Methods). High |CCFM| indicates activity related to locomotion (for example, Fig. 2e), and high CCFF indicates visually driven activity.

As in Fig. 2f, swimming behaviour of most fish became erratic during open-loop stimulus replay. This observation shows that the behavioural state of an animal strongly depends on the presence of appropriate sensory feedback following a motor command.

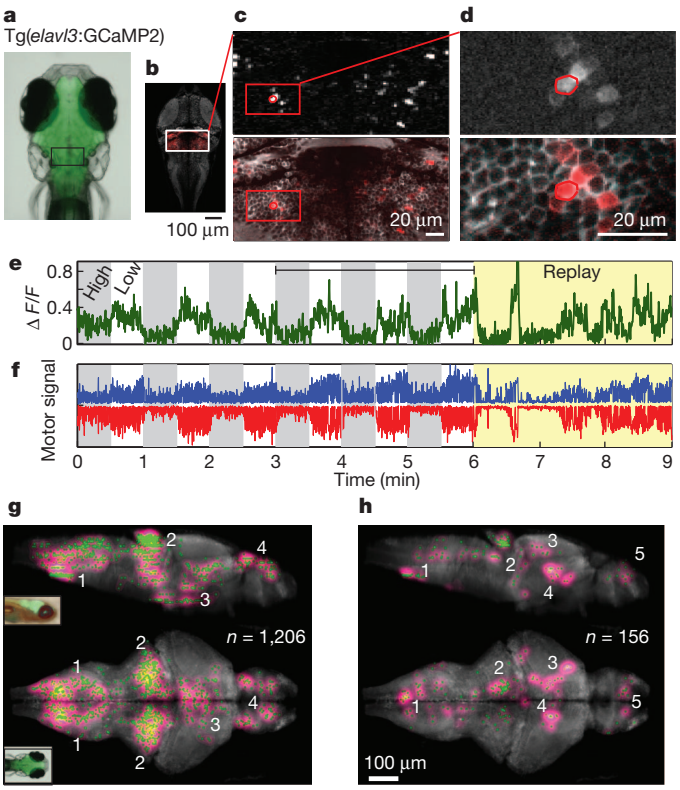

Figure 2 | Functional imaging during adaptive motor control in larval zebrafish. **a**, Micrograph of a transgenic larval zebrafish with pan-neuronal GCaMP2 expression under control of the *elavl3* promoter. The area scanned in **c**–**e** is indicated by a box. **b**, Automatic localization of imaged plane on a reference brain (Methods). **c**, Detected signal (top; Methods) overlaid on anatomical image (bottom). The neuron of interest selected in **d** and **e** is indicated by a red circle. **d**, Correlational map (top, correlation coefficient of ROI signal with all pixels in the red rectangle; Methods) overlaid on anatomy (bottom). The example neuron has been hand segmented. **e**, Fluorescence time series of example neuron. Grey, high feedback gain; white, low feedback gain. Yellow, open-loop stimulus playback from the previous 3 minutes (black bar). **f**, Fictive locomotor drive is boosted during low gain periods. The fluorescence time series in **e** is strongly correlated with the fictive swim signal (yellow replay period: $|CCFM = 0.58| > CCFF = 0.21$). **g**, Areas in the brain with activity strongly correlating to fictive locomotion ($|CCFM| > 0.5$; *n* is the number of sites satisfying the criterion). Green dots, location of identified sites; magenta–yellow gradient, spatial uncertainty (caused by mapping 32 brains to one reference brain), scaled by sampling density. Units were found in 1, areas of the hindbrain, including the inferior olive; 2, in the cerebellum and anterior hindbrain; 3, in the NMLF and pretectum area; 4, in the forebrain. Top panel, side view; bottom panel, top view. **h**, Areas correlating with visual stimulation but not motor output ($CCFF > |CCFM|$, $CCFF > 0.2$; Methods). 1, hindbrain; 2, cerebellum; 3, tectum; 4, pretectum; 5, forebrain. Top panel, side view; bottom panel, top view.

Figure 2g shows the density of neurons in the reference brain ($n = 32$ fish) whose activity was strongly correlated to fictive motor output during replay (high |CCFM|; Methods). Clusters of such neurons can be seen in the caudal hindbrain, including the inferior olive, in the cerebellum, near the nucleus of the medial longitudinal fasciculus (NMLF) and pretectum, and in the forebrain. Asymmetries in the anatomical maps may arise from the limited sensitivity of GCaMP2 and the limited sampling of the brain. Figure 2h shows the density of neurons whose activity correlates with visual input (high CCFF; Methods). Here we used a more liberal criterion because only a small fraction of all possible visual input could be sampled, so that this map is by necessity less complete than that in Fig. 2g. Nevertheless, densities were found in the area of the pretectum, the tectum, the cerebellum and the hindbrain (including the inferior olive). Thus, regions throughout the brain that are involved

in locomotion could be identified through correlational analysis of neural activity during behaviour.

Phase-space representation of network activity

As a first step towards understanding the dynamics that occur during motor adaptation, activity of all identified sites across all fish was visualized by embedding it in a three-dimensional phase space using principal components analysis (PCA)[32,33] (traces averaged over six low–high gain repetitions; see Methods).

As expected, the trajectory loops back to the starting point (Fig. 3a, c), reflecting the periodicity of the neural activity induced by the paradigm, which consisted of repeating periods of high and low feedback gain. The velocity through the principal component space is initially high after a change in feedback gain, then slows down (Fig. 3d) to reach one of two approximately-steady states (β and δ in Fig. 3c). Notably, the periods of fast change in network space (α and γ) coincide with the period of behavioural change (Fig. 1g). Indeed, the first two temporal principal components shown in Fig. 3b reflect steady-state activity (TCP1) and transient activity (TCP2) after a decrease in feedback gain. In summary, network activity evolves quickly following a change in feedback gain, and then settles into one of two steady states depending on the setting of the feedback gain. Network changes coincide with changes in behaviour, and steady network states correspond to periods of stable behaviour. To determine what neural activity induces the two transient and the two steady phases, we next looked for neurons that showed correlated activity with these four phases, that is, during the four phases α–δ in Fig. 3d.

Neural correlates of adaptive motor control

Motor-related neurons (phase β)

Neurons exhibiting raised activity during the low-gain, high-locomotor-drive phase were termed 'motor' related neurons (average fluorescence $F_\beta > F_\delta$, paired t-test on six repetitions, $P < 0.005$). The neurons of Figs 2e and 4a are two examples. Activity of these two neurons was more related to locomotion than to visual input, as determined by |CCFM| > CCFF during replay (Fig. 2e: |CCFM = 0.58| > CCFF = 0.21, Fig. 4a: |CCFM = 0.154| > CCFF = 0.052). This was the case for almost all members of the 'motor' population (Fig. 4g). The population average of activity of 'motor' neurons is shown in Fig. 4f.

'Motor' units were found in areas shown in Fig. 5a: in the posterior hindbrain[34,35], with a particularly dense concentration just caudal to the cerebellum, and in the inferior olive; in the reticulospinal system (Supplementary Fig. 6), as suggested by previous studies[24,25]; throughout the cerebellum, particularly in the corpus, including in areas of the Purkinje (larger, more dorsal cell bodies) and in granule cell (smaller, deeper cell bodies) layers[36–38], and in the deep cerebellum (more lateral); in the midbrain, ventral to the optic tectum, near the NMLF and in the pretectum[38,39]; in the habenula; and in the pallium.

Gain-decrease-related neurons (phase α)

Neuronal populations that are active after a decrease in gain may be responsible for driving the animal into a state of high locomotor drive. Signals during this period are also consistent with the detection of discrepancies between expected and received visual feedback, which are thought to drive many forms of adaptive behaviour[10,11,12,31,40,41]. An example from the 'gain-down' population ($F_\alpha > F_\beta$, $F_\alpha > F_\delta$; two t-tests on six gain repetitions, $P < 0.005$), at the ventrolateral border of the cerebellum, is shown in Fig. 4b: after a gain decrease, this neuron shows transient activity that returns to baseline while the increase in locomotor drive is maintained. The stimulus replay period shows that the neuron is not visually driven, but is instead functionally related to motor output (|CCFM = 0.32| > CCFF = 0.15), as are most other neurons of this population (Fig. 4g).

Gain-down units were found in the cerebellum and in the inferior olive (Fig. 5b). In the cerebellum they appeared in both the areas of the Purkinje and granule cell layers, and in the deep cerebellum. In the dorsal areas they appeared medial, and in the deep cerebellum they appeared lateral. The anatomical localization of gain-down units to the cerebellum is consistent with findings in mammals, in which the cerebellum is a locus of motor learning[10,11]. Some units were also found in the hindbrain just caudal to the cerebellum.

Gain-increase-related neurons (phase γ)

Figure 4c shows calcium signals of a 'gain-up' neuron in the optic tectum that shows transient signals after an increase in gain ($F_\gamma > F_\beta$, $F_\gamma > F_\delta$). This neuron is mainly driven by visual input , as the calcium trace during the replay period resembles the trace during the matched preceding period (|CCFM = –0.21| < CCFF = 0.59, representative of the population, see Fig. 4g). Not many neurons with the gain-up property were found ($n = 39$), but a concentration was found in the inferior olive (Fig. 5b), and most of these neurons were visually driven (Fig. 4g).

Motor-off-related neurons (phase δ)

A fourth class of neurons showed raised activity during periods of weak locomotion or absence of locomotion, termed the 'motor-off' class ($F_\delta > F_\beta$). Figure 4d shows an example of such a neuron, in the dorsal hindbrain, whose activity is elevated during periods of high gain and low locomotor drive. Notably, during the stimulus replay period, the calcium signal still peaks during periods of no swimming, indicating that this is a motor-related neuron instead of a visually driven neuron (|CCFM = –0.40| > CCFF = 0.18). It might be involved in inhibiting motor output, or in suppressing behaviours that should not be executed during vigorous swimming. Not all motor-off neurons had this property; some were more visually driven (Fig. 4g).

Motor-off units were concentrated in the dorsal hindbrain (Fig. 5d), in the cerebellum, in the inferior olive, in the ventral midbrain near the NMLF and the pretectum, and in the habenula and pallium.

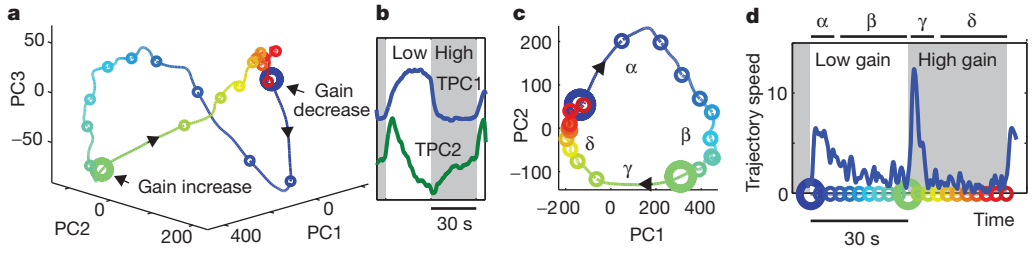

Figure 3 | Low-dimensional representation of neural network dynamics. **a**, Projection of activity of all detected units from all fish onto the first three principal components (PC1, PC2 and PC3) derived from principal components analysis. Circles, intervals of three seconds. **b**, First two temporal principal components (TPCs). TPC1 shows elevated activity during low gain periods; TCP2 shows transient activity after a gain decrease followed by a slow dip (see Supplementary Figs 20 and 21). **c**, Top view of **a** (α, transient dynamics after switch to low gain; β, steady state during low gain; γ, transient dynamics after switch to high gain; δ, steady state during high gain). **d**, Speed through phase space over one low-high gain period, showing accelerated trajectory speed after gain changes. Colours in **a**–**d** represent time points as shown on the x axis of **d**.

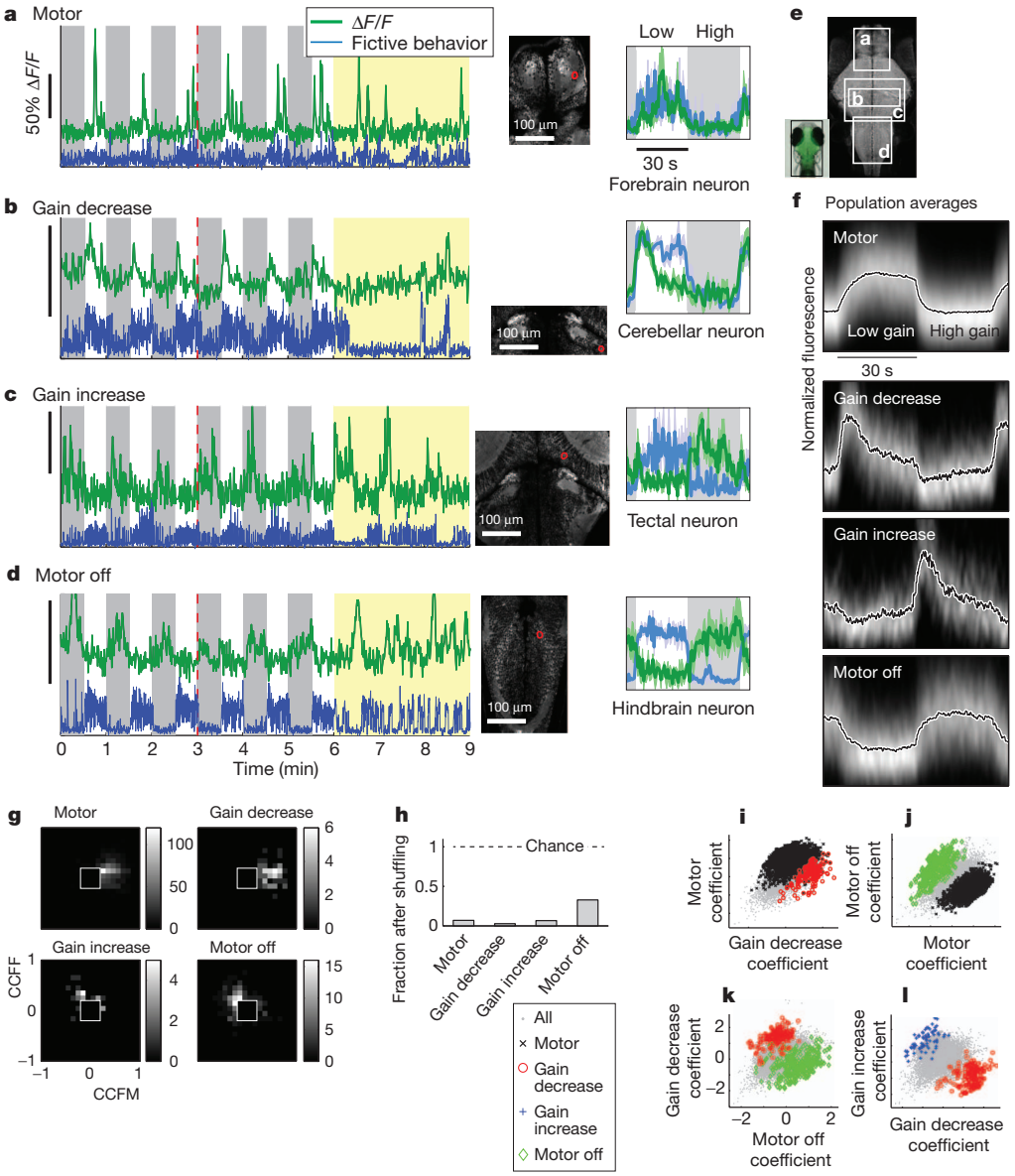

Figure 4 | Four types of neural dynamics during adaptive motor control. **a**–**d**, Motor-related activity in a single neuron in the forebrain (**a**), transient activity after decreases in gain in a neuron in the deep cerebellum (**b**), transient activity after increases in gain in a visually driven neuron in the tectum (**c**), and motor-off activity in a neuron in the dorsal hindbrain (**d**). Left panels: white, low gain periods; grey, high gain periods; yellow, stimulus replay period from the previous 3 minutes (the start of the replayed portion is indicated by the dashed red line); blue, fictive swim signals; green, single-neuron fluorescence signal. Scale bars, 50% Δ*F*/*F*. Middle panels, imaged plane (the neuron is outlined in red). Right panels, fluorescence traces (green) and behaviours (blue), averaged over six gain repetitions, with standard errors (light green and light blue). **e**, anatomical locations of recordings in **a**–**d**. **f**, Population data for neuron types as in **a**–**d**, with normalized averages (black) overlaid on a heat map of individual traces. **g**, Histograms of CCFM and CCFF. Neurons in the motor and gain-down groups are more related to locomotion; neurons in the gain-up group are more responsive to visual input, and the motor-off group is mixed. The empty square in the centre represents values of CCFM and CCFF that are indistinguishable from those arising from noise (see Supplementary Figs 17 and 18). **h**, Control for false positives. When fluorescence traces are scrambled by cutting at 16 random time points and rearranging, the number of detected units falls by a factor of 8.1 on average, indicating that detected units are not a result of false positives (chance level is at 1). **i**, Scatter plot of motor coefficient (average normalized fluorescence during seconds 10–30 of low gain period) versus gain-down coefficient (average fluorescence during seconds 1–8 of low gain period) showing segregation with partial overlap of motor and gain-down units. **j**–**l**, Similar scatter plots to **i** but for other coefficients. No detected neuron codes for both upwards and downwards gain changes (**l**): transient neuronal activity is specific to the direction of gain change.

Correlation-based maps of sites strongly correlating or anticorrelating with locomotion during replay (Fig. 5e, f), as measured using CCFM, are generally consistent with maps of the anatomical locations of 'motor' neurons and motor-off neurons (Fig. 5a, d), and reveal additional structures such as two arcs in the dorsal hindbrain.

Population averages summarizing the above four types of neural dynamics are shown in Fig. 4f (individual traces are shown in Supplementary Figs 13–16). The detected units were not false positives resulting from noisy measurements of neural activity, and this is confirmed by shuffling the fluorescence time series, which causes an eightfold drop in detected units (Fig. 4h, Methods). Figure 4i–l shows that neurons generally only belong to one functional class, but there is some overlap between motor and gain-down neurons (46% of gain-down units also have sustained activity during low gain), and no overlap between gain-down and gain-up units, consistent with previously observed asymmetries between gain adaptation in opposite directions[42]. Supplementary Movie 4 contains anatomical stacks with superimposed clusters of the functionally identified neural classes (same data as Fig. 5). As GCaMP2 has a relatively weak signal-to-noise ratio, and as the brain was sampled a

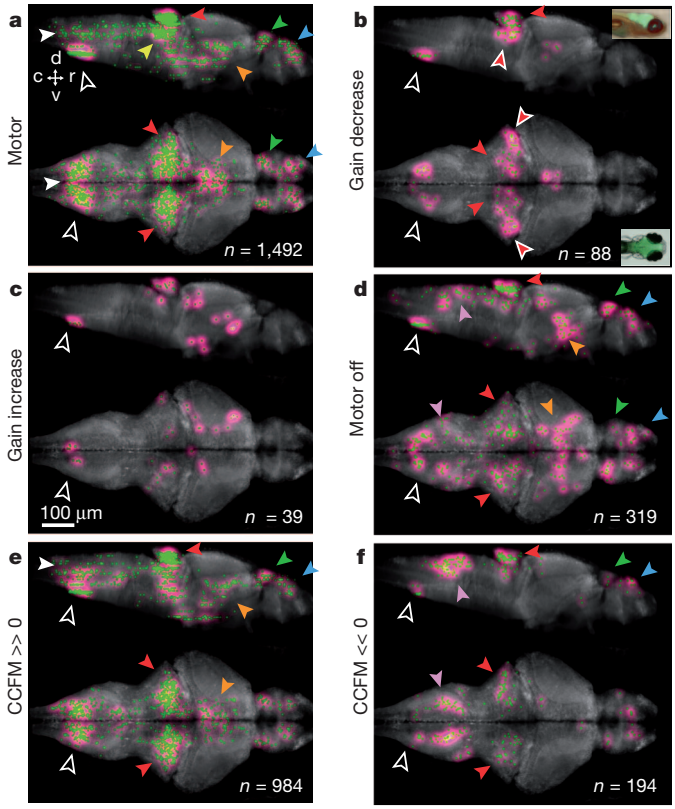

Figure 5 | Anatomical locations of neurons and neuropil regions. **a–d,** Anatomical locations are classified by the statistical criteria described in the text (32 fish, normalized by sampling density; see also Supplementary Figs 9–12). **a**, 'Motor' neurons. **b**, Gain decrease neurons, **c**, Gain increase neurons. **d**, Motor-off neurons. Green dots, locations of identified sites; magenta, confidence interval scaled by sampling density (Methods). **e**, Sites with activity relating to locomotion as measured during replay by CCFM > 0.4. **f**, Sites anticorrelating with locomotion, as measured by CCFM < -0.25. Black arrows with white outline, inferior olive; red arrows, cerebellum; red arrows with white outline, deep lateral cerebellum; yellow arrow, ventral hindbrain nearby cerebellum; white arrows, posterior hindbrain; pink arrows, dorsal posterior hindbrain; orange arrows, NMLF and pretectum area; green arrows, habenula; blue arrows, pallium.

limited number of times, the anatomical maps are not exhaustive, so we quantified the uncertainty in detecting or missing functional units (Supplementary Fig. 10).

Thus, the four types of neural dynamics identified via a dimensionally reduced representation of network activity could be mapped to distinct brain areas. To the best of our knowledge, this is the first brain-wide imaging at the cellular level of activity related to adaptive motor control in a vertebrate brain.

Discussion

The ability to monitor neural activity at single-cell resolution throughout the whole brain of a behaving animal creates new opportunities for studying circuit function during behaviour. The demonstration that paralysed larval zebrafish interact readily with a virtual environment, and the remarkable finding that these animals still showed short-term forms of motor learning in the fictive virtual-reality setup, provided an exciting opportunity to study the circuit dynamics occurring during this behaviour.

Here we identified neural populations activated during specific phases of adaptive locomotion that span multiple areas of the larval zebrafish brain. Both the inferior olive and the cerebellum contained many neurons correlating with adaptive motor control. In mammals, cerebellar circuits play an important role in motor control[11] and in fish the cerebellum has been shown to be involved in the selection of motor programs[43–45]. Furthermore, the structure of olivocerebellar circuitry in zebrafish is remarkably similar to that of mammals[36,37,46] (Supplementary Fig. 23a), and the transient gain-down activity observed in the inferior olive and cerebellum may represent error signals driving motor learning mechanisms[11,40,41,47].

To test whether the inferior olive is necessary for motor adaptation, we next lesioned it with an infrared laser[24]. Post lesion, the power of swim bouts in the high- and low-gain settings became statistically indistinguishable (Fig. 6). Although damage to passing axons cannot be ruled out, similar lesions in the dorsal anterior hindbrain did not affect motor adaptation ($P < 0.001$ pre lesion; $P = 0.01$ post lesion; Fig. 6c and Supplementary Fig. 28). The optomotor response was still intact (Supplementary Fig. 24). These results indicate that the inferior olive is necessary for successful adaptation of motor programs to external feedback gain. One possibility is that an error signal is computed in the inferior olive through subtractive interaction of an efference copy of motor output (for example, through inhibitory connections from premotor circuits) and visual feedback from a swim bout (for example, through pretectal projections; see also Supplementary Fig. 27), which then activates appropriate circuits in the cerebellum via climbing fibres. Cerebellar activity may drive changes in motor programs through the deep cerebellum, which in mammals projects to premotor circuits.

Although synaptic plasticity underlies much of motor learning[11,12], it is only one of several candidate mechanisms for the behaviour observed here. An alternative idea is that sustained firing rates of neuronal populations, perhaps subsets of the motor and motor-off populations, implement and maintain the different levels of locomotor drive over prolonged periods; for example, through attractor states[48].

The function of the observed adaptive sensorimotor behaviour may be multifold. On long timescales, development of muscle and body shape will require continuous adjustment of sensorimotor control. On medium timescales, fluctuating body mass due to eating, and fluctuating viscosity of the water require some adaptation of swimming behaviour. In addition, temperature fluctuations cause changes in muscle efficacy[49] that must be counterbalanced by adjustments of locomotor drive. On short timescales, the relationship between the speed of optic flow following a swim bout depends on the distance to the optical surround (objects farther away induce smaller optic flow), requiring recalibration of the sensorimotor loop on the timescale of seconds. In our experiments, we observed adaptation occurring on such a timescale. Human motor control faces many similar challenges and is subject to continuous recalibration to cope with changing conditions (for example, leg injury, walking on a slippery floor or carrying a heavy bag). Thus, the current study of brain-wide activity during adaptive locomotion is an important step towards understand-

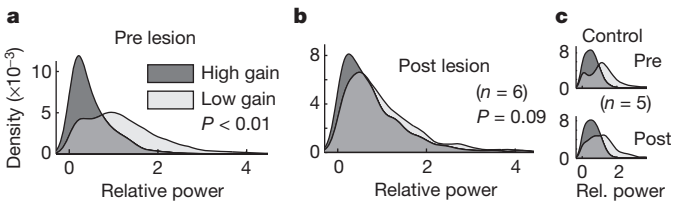

Figure 6 | Effect of inferior olive lesions on visually induced motor adaptation. **a**, Histogram of power per swim bout in the high- and low-gain conditions for six fish, pre lesion. Difference in mean power per fish is significant before lesion ($P < 0.001$, t-test on means of $n = 6$ fish). **b**, Post-lesion histogram. The inferior olive was lesioned in approximately 60 locations with an infrared laser. The fish still performed the optomotor response (Supplementary Fig. 24), but the power of the swim bouts was not no longer adjusted significantly to the external feedback gain ($P = 0.09$, same six fish). **c**, Lesions of similar size in the dorsal anterior hindbrain did not impair motor adaptation ($P < 0.001$ pre lesion for $n = 5$ fish, $P = 0.01$ post lesion, Supplementary Figs 23 and 28). These results indicate that the inferior olive is a necessary component of the circuit driving motor adaptation.

ing entire circuits in the precise context for which they evolved: the flexible control of behaviour in changing environments.

METHODS SUMMARY

Larval zebrafish fictively swam in a one-dimensional virtual environment, while neuronal activity was monitored using a two-photon microscope.

Full Methods and any associated references are available in the online version of the paper at www.nature.com/nature.

Received 16 June 2011; accepted 15 March 2012.
Published online 9 May 2012.

1. Wall, P. D., Freeman, J. & Major, D. Dorsal horn cells in spinal and in freely moving rats. *Exp. Neurol.* **19,** 519–529 (1967).
2. Flusberg, B. A. *et al.* High-speed, miniaturized fluorescence microscopy in freely moving mice. *Nature Methods* **5,** 935–938 (2008).
3. Naumann, E. A., Kampff, A. R., Prober, D. A., Schier, A. F. & Engert, F. Monitoring neural activity with bioluminescence during natural behavior. *Nature Neurosci.* **13,** 513–520 (2010).
4. Dombeck, D. A., Harvey, C. D., Tian, L., Looger, L. L. & Tank, D. W. Functional imaging of hippocampal place cells at cellular resolution during virtual navigation. *Nature Neurosci.* **13,** 1433–1440 (2010).
5. Maimon, G., Straw, A. D. & Dickinson, M. H. Active flight increases the gain of visual motion processing in *Drosophila*. *Nature Neurosci.* **13,** 393–399 (2010).
6. Seelig, J. D. *et al.* Two-photon calcium imaging from head-fixed *Drosophila* during optomotor walking behavior. *Nature Methods* **7,** 535–540 (2010).
7. Fry, S. N., Rohrseitz, N., Straw, A. D. & Dickinson, M. H. Visual control of flight speed in *Drosophila melanogaster*. *J. Exp. Biol.* **212,** 1120–1130 (2009).
8. Möhl, B. Short-term learning during flight control in *Locusta migratoria*. *J. Comp. Physiol.* **163,** 803–812 (1988).
9. Wolf, R., Voss, A., Hein, S., Heisenberg, M. & Sullivan, G. D. Can a fly ride a bicycle? *Phil. Trans. R. Soc. Lond. B* **337,** 261–269 (1992).
10. du Lac, S., Raymond, J. L., Sejnowski, T. J. & Lisberger, S. G. Learning and memory in the vestibulo-ocular reflex. *Annu. Rev. Neurosci.* **18,** 409–441 (1995).
11. Raymond, J. L., Lisberger, S. G. & Mauk, M. D. The cerebellum: a neuronal learning machine? *Science* **272,** 1126–1131 (1996).
12. Gilbert, P. F. & Thach, W. T. Purkinje cell activity during motor learning. *Brain Res.* **128,** 309–328 (1977).
13. Körding, K. P. & Wolpert, D. M. Bayesian integration in sensorimotor learning. *Nature* **427,** 244–247 (2004).
14. Portugues, R. & Engert, F. Adaptive locomotor behavior in larval zebrafish. *Front. Syst. Neurosci.* **5,** 72 (2011).
15. Rock, I. & Smith, D. The optomotor response and induced motion of the self. *Perception* **15,** 497–502 (1986).
16. Orger, M. B., Smear, M. C., Anstis, S. M. & Baier, H. Perception of Fourier and non-Fourier motion by larval zebrafish. *Nature Neurosci.* **3,** 1128–1133 (2000).
17. Gahtan, E., Sankrithi, N., Campos, J. B. & O'Malley, D. M. Evidence for a widespread brain stem escape network in larval zebrafish. *J. Neurophysiol.* **87,** 608–614 (2002).
18. Ohki, K., Chung, S., Ch'ng, Y. H., Kara, P. & Reid, R. C. Functional imaging with cellular resolution reveals precise micro-architecture in visual cortex. *Nature* **433,** 597–603 (2005).
19. Denk, W., Strickler, J. H. & Webb, W. W. Two-photon laser scanning fluorescence microscopy. *Science* **248,** 73–76 (1990).
20. Higashijima, S.-I., Masino, M. A., Mandel, G. & Fetcho, J. R. Imaging neuronal activity during zebrafish behavior with a genetically encoded calcium indicator. *J. Neurophysiol.* **90,** 3986–3997 (2003).
21. Bene, F. D. *et al.* Filtering of visual information in the tectum by an identified neural circuit. *Science* **330,** 669–673 (2010).
22. Douglass, A. D., Kraves, S., Deisseroth, K., Schier, A. F. & Engert, F. Escape behavior elicited by single, channelrhodopsin-2-evoked spikes in zebrafish somatosensory neurons. *Curr. Biol.* **18,** 1133–1137 (2008).
23. Chong, M. and Drapeau, P. Interaction between hindbrain and spinal networks during the development of locomotion in zebrafish. *Dev. Neurobiol.* **67,** 933–947 (2007).
24. Orger, M. B., Kampff, A. R., Severi, K. E., Bollmann, J. H. & Engert, F. Control of visually guided behavior by distinct populations of spinal projection neurons. *Nature Neurosci.* **11,** 327–333 (2008).
25. O'Malley, D. M., Kao, Y. H. & Fetcho, J. R. Imaging the functional organization of zebrafish hindbrain segments during escape behaviors. *Neuron* **17,** 1145–1155 (1996).
26. Dombeck, D. A., Khabbaz, A. N., Collman, F., Adelman, T. L. & Tank, D. W. Imaging large-scale neural activity with cellular resolution in awake, mobile mice. *Neuron* **56,** 43–57 (2007).
27. Masino, M. A. & Fetcho, J. R. Fictive swimming motor patterns in wild type and mutant larval zebrafish. *J. Neurophysiol.* **93,** 3177–3188 (2005).
28. Cohen, A. H. & Wallén, P. The neuronal correlate of locomotion in fish. "fictive swimming" induced in an *in vitro* preparation of the lamprey spinal cord. *Exp. Brain Res.* **41,** 11–18 (1980).
29. Tallini, Y. N. *et al.* Imaging cellular signals in the heart *in vivo*: cardiac expression of the high-signal Ca^{2+} indicator GCaMP2. *Proc. Natl Acad. Sci. USA* **103,** 4753–4758 (2006).
30. Park, H. C. *et al.* Analysis of upstream elements in the *Hu*C promoter leads to the establishment of transgenic zebrafish with fluorescent neurons. *Dev. Biol.* **227,** 279–293 (2000).
31. Ito, M., Shiida, T., Yagi, N. & Yamamoto, M. Visual influence on rabbit horizontal vestibulo-ocular reflex presumably effected via the cerebellar flocculus. *Brain Res.* **65,** 170–174 (1974).
32. Mazor, O. & Laurent, G. Transient dynamics versus fixed points in odor representations by locust antennal lobe projection neurons. *Neuron* **48,** 661–673 (2005).
33. Yaksi, E., von Saint Paul, F., Niessing, J., Bundschuh, S. T. & Friedrich, R. W. Transformation of odor representations in target areas of the olfactory bulb. *Nature Neurosci.* **12,** 474–482 (2009).
34. Kinkhabwala, A. *et al.* A structural and functional ground plan for neurons in the hindbrain of zebrafish. *Proc. Natl Acad. Sci. USA* **108,** 1164–1169 (2011).
35. Koyama, M., Kinkhabwala, A., Satou, C., Higashijima, S.-I. & Fetcho, J. Mapping a sensory-motor network onto a structural and functional ground plan in the hindbrain. *Proc. Natl Acad. Sci. USA* **108,** 1170–1175 (2011).
36. Bae, Y.-K. *et al.* Anatomy of zebrafish cerebellum and screen for mutations affecting its development. *Dev. Biol.* **330,** 406–426 (2009).
37. Kani, S. *et al.* Proneural gene-linked neurogenesis in zebrafish cerebellum. *Dev. Biol.* **343,** 1–17 (2010).
38. Volkmann, K., Chen, Y.-Y., Harris, M. P., Wullimann, M. F. & Köster, R. W. The zebrafish cerebellar upper rhombic lip generates tegmental hindbrain nuclei by long-distance migration in an evolutionary conserved manner. *J. Comp. Neurol.* **518,** 2794–2817 (2010).
39. Wullimann, M. F., Rupp, B. & Reichert, H. *Neuroanatomy of the Zebrafish Brain: a Topological Atlas* (Birkhäuser, 1996).
40. Marr, D. A theory of cerebellar cortex. *J. Physiol.* **202,** 437–470 (1969).
41. Albus, J. A theory of cerebellar function. *Math. Biosci.* **10,** 25–61 (1971).
42. Boyden, E. S. & Raymond, J. L. Active reversal of motor memories reveals rules governing memory encoding. *Neuron* **39,** 1031–1042 (2003).
43. Matsumoto, N., Yoshida, M. & Uematsu, K. Effects of partial ablation of the cerebellum on sustained swimming in goldfish. *Brain Behav. Evol.* **70,** 105–114 (2007).
44. Roberts, B. L., van Rossem, A. & de Jager, S. The influence of cerebellar lesions on the swimming performance of the trout. *J. Exp. Biol.* **167,** 171–178 (1992).
45. Aizenberg, M. & Schuman, E. M. Cerebellar-dependent learning in larval zebrafish. *J. Neurosci.* **31,** 8708–8712 (2011).
46. Ma, L., Punnamoottil, B., Rinkwitz, S. & Baker, R. Mosaic *hoxb4a* neuronal pleiotropism in zebrafish caudal hindbrain. *PloS ONE* **4,** e5944 (2009).
47. De Zeeuw, C. I. *et al.* Microcircuitry and function of the inferior olive. *Trends Neurosci.* **21,** 391–400 (1998).
48. Miri, A. *et al.* Spatial gradients and multidimensional dynamics in a neural integrator circuit. *Nature Neurosci.* **14,** 1150–1159 (2011).
49. Bennett, A. F. Temperature and muscle. *J. Exp. Biol.* **115,** 333–344 (1985).

Supplementary Information is linked to the online version of the paper at www.nature.com/nature.

Acknowledgements We are grateful to D. Schoppik for teaching M.B.A. the fictive swimming preparation, to K.-H. Huang for carrying out spinal calcium green injections, and to M. Concha, R. Baker and L.-H. Ma for advice on anatomy. We thank M. Meister, B. Ölveczky, D. Wolpert, E. Mukamel, M. Yartsev, D. Schoppik, D. Hildebrand, E. Naumann, A. Kampff, P. Latham, T. Dunn and members of the Engert laboratory for useful discussions and comments on the manuscript. We thank P. Oteiza and R. Hellmiss for help with anatomy and figures, and A. Viel for use of laboratory space. M.B.A. thanks D. Wolpert and E. Santos for support. This work was supported by a Sir Henry Wellcome Fellowship from the Wellcome Trust (M.B.A.), a K99 grant no. 5K99NS62780-2 (M.B.O.) and National Institutes of Health grants 5R01EY014429 and RC2NS069407 (F.E.).

Author Contributions M.B.A. developed the fictive virtual-reality paradigm, carried out the experiments, analysed the data, and built the setup and software. M.B.A., F.E. and R.P. conceived the experiments. M.B.O., D.N.R., J.M.L. and A.F.S. generated the transgenic *elavl3*:GCaMP2 fish line. M.B.O. generated the transgenic alpha tubulin:C3PA–GFP fish line. All authors discussed the data and the manuscript. M.B.A. wrote the manuscript with the assistance of R.P., M.B.O. and F.E.

Author Information Reprints and permissions information is available at www.nature.com/reprints. The authors declare no competing financial interests. Readers are welcome to comment on the online version of this article at www.nature.com/nature. Correspondence and requests for materials should be addressed to F.E. (florian@mcb.harvard.edu).

METHODS

Fictively driven virtual environment. Wild-type larvae of the WIK strain were used for behavioural experiments. For reticulospinal imaging, nacre fish on a WIK background were used, and for two-photon imaging, nacre fish expressing GCaMP2 under control of the *elavl3* promoter (refs 20, 30) were used, again on a WIK background. All experiments were approved by the Standing Committee on the Use of Animals in Research and Training of Harvard University. Zebrafish larvae of 6 or 7 d.p.f. were briefly anaesthetized with MS222 and paralysed by injection with a 1 mg ml^{-1} bungarotoxin solution (Sigma-Aldrich), then suspended from structural pipettes (Supplementary Fig. 3) or embedded in agarose but with the agarose around the tail removed. Motor nerve recordings were made with a Multiclamp 700B amplifier, simultaneously with two-photon imaging. Experiments were done at room temperature in filtered facility fish water. Visual scenes were projected onto a diffusive screen underneath the Petri dish containing the fish, using a mini projector whose light source was replaced by a red Luxeon Rebel light-emitting diode (LED) that was pulsed in synchrony with the fast scan mirror, so that illumination only occurred at the edges of the image where the scan mirror changed direction (typically at 800 Hz) to avoid any corruption of the two-photon images. Visual scenes consisted of square gratings with spatial period 12 mm moving at 1 cm s^{-1} from tail to head in the absence of motor nerve signals (-1 cm s^{-1}). When the processed swim signal was above an automatically set threshold (see Supplementary Methods and Supplementary Fig. 2), the locomotor drive was defined as the area underneath the curve of the processed swim signal during the current and the previous video frame. The processed swim signal was defined as the standard deviation of the raw swim signal in a sliding window of 15 ms (see Fig. 1d). In the presence of such motor nerve signals, the instantaneous virtual-fish velocity was set, 60 times per second (at the rate of the 60-Hz projector), to -1 cm s^{-1} + (gain × instantaneous locomotor drive), with the gain set experimentally, after which the velocity decayed back to -1 cm s^{-1} at a rate of -15 cm s^{-2}, approximately matched to freely swimming fish dynamics (Supplementary Fig. 1). The high gain was chosen to be two to five times higher than the low gain, and these values bracketed the 'natural' gain setting that described the transformation of motor activity into optic flow in a freely swimming fish. The high- and low-gain settings were manually adjusted for each fish, as different fish showed different ranges of adaptability. Some fish showed a transient increase in fictive motor output followed by a decrease after a gain-down change; these fish were discarded from the gain-down data set because transient neural activity could not be distinguished from motor-related activity (rejection criterion: $P < 0.03$, paired t-test on fictive signal averages over seconds 0–15 versus averages over seconds 15–30 after gain-down change).

Generation of transgenic fish. To generate the transgenic line Tg(-1.7Ca*Tuba*:C3PA-GFP) the C3PA-GFP open reading frame and polyadenylation sequence[50] was PCR amplified using the primers cttttgccttttttcttc acagGTGAGCAAGGGCGAGGAGC (forward, coding sequence upper case) and GGggatccTGGACAAACCACAACTAG (reverse) and fused in a second PCR step to the goldfish α1-tubulin *cis*-regulatory sequence[51], and first exon and intron amplified with the forward primer ggACGCGTgctcccggactcagatc and complementary reverse primer GCTCCTCGCCCTTGCTCACCtgtgaagaaaa aggcaaaag, resulting in an in frame replacement of the α-tubulin coding sequence with C3PA-GFP. This cassette was cloned into a plasmid with Tol2 arms using restriction enzymes Mlu1 and BamH1. The transgenic line Tg(*elavl3*:GCaMP2) was made by first cloning GCaMP2 downstream of an AttR1-R2 cassette flanked by Tol2 arms, and then placing it under the control of *elavl3* (*HuC*) *cis*-regulatory sequences including the first exon with the start codon mutated, and first intron[20] via L/R recombination with an AttL flanked *elavl3* entry clone. The resulting plasmids were injected into 1-cell-stage embryos at a concentration of 20 ng µl^{-1} in combination with Tol2 transposase RNA at a concentration of 25 ng µl^{-1}. Founders were selected based on high and spatially uniform expression.

Two-photon microscopy. A custom-built laser scanning two-photon microscope, using a Spectra Physics Mai Tai pulsed infrared laser, was used to monitor fluorescence in the brain. A photomultiplier tube (PMT) with a green bandpass filter and a laser-blocking filter was used to monitor green fluorescence. The fish was illuminated from below by a near-infrared LED light source whose light path was combined with the light path of the projector using a dichroic mirror (a 'hot mirror', Edmund Optics; not shown in Fig. 1). The image of the fish was registered above the objective using another dichroic mirror by a camera (AVT Stingray). Areas of the brain were scanned at 1.5 to 3 Hz, typically with 4–8 µm between imaging planes. Fish typically showed robust behaviour for a period of 3–5 h, so that not the entire brain of every fish could be scanned (although almost 100% coverage was possible in some fish). Thirty-two fish were used to non-homogeneously cover six times the volume of the brain (see Supplementary Fig. 9). The electrophysiology, stimulus presentation and the two-photon microscope were controlled by a single piece of software custom written in C# (Microsoft). Two data acquisition cards (National Instruments) were used to acquire imaging and electrophysiology data, and were synchronized using periodic digital pulses.

Analysis of the two-photon images. Image analysis software was written in Matlab (Mathworks). We developed a novel method for automatically extracting regions of interest from two-photon movies that contain many neurons. A square ROI, half the size of a neuron, is swept over all locations of the imaging plane. At each location, a fluorescence time series, averaged over the ROI, is extracted and converted to a statistic for the 'peaky-ness' of the fluorescence signal at that point. If $f_{x,y}(t)$ is the fluorescence of the pixel at x, y at time t, and $f_{x,y}$ is the average fluorescence at pixel x, y, and f is the average of $f_{x,y}$, then the statistic is defined as:

$$m_{x,y} = \left\langle \left\langle \left(f_{x,y}(t) - f_{x,y}\right) / \left(f_{x,y} + f\right) \right\rangle_{ROI}^{3} \right\rangle_{t}$$

where $\langle \ldots \rangle_{\mathrm{ROI}}$ denotes the spatial average over the ROI and $\langle \ldots \rangle_t$ means average over time. This measure was chosen because it bears a resemblance to the usual $\Delta F/F$ but contains an offset to counteract the undesirable amplification of noise in areas of low fluorescence; the third power was chosen because it nonlinearly converts peaks in the fluorescence signal to larger values of the statistic. This measure—one of several tested—yielded spatial signal maps $m_{x,y}$, which tended to be at least as sensitive as sets of ROIs selected manually from observation of the raw and $\Delta F/F$ movies. In general, the maps were also more complete than ROIs obtained using PCA and independent component analysis (ICA) methods[50], which detected large events in which many neurons participated, but often missed small, sparse activation of single neurons. Thus, a spatial map of activity is obtained as in the top panel of Fig. 2c. This map is smoothed by convolution with a Gaussian function the size of a neuron, and the maxima are designated as points of interest. Points that were less than a cell-body length away from one another, including 'chains' of such points, which sometimes occurred in regions of activated neuropil, were pruned to a single point at the centre using an automated procedure. These points of interest formed the centre of new ROIs and were found to be positioned at the centre of neurons in the majority of cases (for example, Fig. 2c). The fluorescence time series of these ROIs formed the basis of the functional classification. The time series could be correlated with the time series of all pixels in a region around the point of interest, leading to a spatial map of correlation coefficients (Fig. 2d, top panel). This method extracted shapes of single neurons because pixel values within a single neuron tend to correlate highly over time. In many cases, the correlational maps also revealed other neurons whose activity was highly correlated with the neuron at the point of interest (Supplementary Fig. 7).

Automatic localization of imaging planes in a reference brain. An entire 6 d.p.f. larval brain (Tg(*elavl3*:GCaMP2) fish treated with 1-phenyl 2-thiourea (PTU) to inhibit eye pigmentation) was scanned and used as a reference brain. Individual imaged planes of other fish were registered onto the reference brain as follows (software was written in Matlab). The reference stack was intensity-normalized per z plane, and thresholded to dampen the effect of brightly labelled neurons on the registration. The peak of the cross-correlation between the mean-subtracted z-planes reference stack and a mean-subtracted image was calculated for each z plane of the reference stack, giving the most likely x and y positions for that z plane (Fig. 2b, Supplementary Fig. 8 and Supplementary Movie 3). The z location was chosen to be the peak of these correlation values, which fixed the x, y and z positions in the entire stack. Manual inspection showed that 82% of images were correctly registered; the remaining images were localized manually. To estimate the accuracy of localization, the reference brain (A) was used as well as a second brain (B). A plane (250 by 270 µm) was randomly selected from brain A, and mapped to brain B by the algorithm. Next, the corresponding plane in brain B was mapped back to A. This was repeated 500 times. Thus, the original location could be compared to the location after two mappings by the algorithm; 500 discrepancies were obtained in this way. The uncertainty in the mapping algorithm was then approximated by the standard deviation of these 500 discrepancies, divided by $\sqrt{2}$ (because two errors accumulate by the double mapping). This was 19.5 µm, so we assumed the slightly higher value of 25 µm for the precision of the algorithm. In 14% of cases, a gross error occurred of greater than 60 µm. These were easily spotted by eye (compare to the manual mapping of our data after gross discrepancies; see above). The unidirectional gross error rate was therefore estimated to be 7%.

As each fish contributed a partial brain to the data set, a total volume of six times the volume of the brain was obtained (assuming a 4-µm z resolution), with certain areas covered more densely than others (see Supplementary Figs 9 and 10). The density maps of Fig. 5 were normalized by the sampling density so that maps were not biased towards the most densely sampled areas. Roughly 1% of all neurons were classified as being active by our activity detection algorithm. Of these, under our statistical criteria, about 20% could be related to the behaviour by

classification into the four groups described in the text. All major clusters in Fig. 5 appeared in more than one fish; neurons were removed if, within a 50-μm sphere, no other neuron within the same class from a different fish was present.

Analysis of neuronal activity. After extracting fluorescence time series from the ROIs (Methods), the traces were analysed in more detail. To distinguish neural activity driven by visual input from activity relating to locomotion, we first smoothed and combined the left and right fictive channel recordings to generate a single quantitative descriptor of motor output, *M*. The motor output and the fluorescence trace were cross-correlated during the replay period (see text) to yield a fluorescence-motor correlation coefficient CCFM. The correlation coefficient of the fluorescence trace during and before replay was termed CCFF. High values of CCFM indicate neural activity relating to locomotion, and high values of CCFF indicate visually driven activity (because the stimulus during replay is a repetition of the preceding stimulus; visually driven neurons should therefore respond in a similar way). In the CCFF versus CCFM histograms (Fig. 4g), there is a region in the centre that cannot be distinguished from noise, which was derived from a fish that did not receive visual input and that did not swim (Supplementary Figs 17 and 18), and which is therefore left blank in the figures.

For dimensionality reduction, principal components of the matrix containing the fluorescence traces of all detected sites (size $n_{\text{sites}} \times n_{\text{time points}}$) were found using the princomp function in Matlab, and consisted of vectors of length n_{sites}. Activity traces from all detected sites, averaged over the six low–high gain repetitions, were projected (by the dot product) onto the first three of these principal components, to obtain three time series (length $n_{\text{time points}}$). These time series served as a 'summary' of activity of all sites across brain regions and fish, as they can be used to approximately reconstruct the activity of the detected sites (using the principal components). The three time series were then visualized by plotting them on three axes, rendering a three-dimensional curve as shown in Fig. 3.

The motor, gain decrease, gain increase and motor-off activity patterns were detected as described in the text. As a large number of units ($n = 9{,}814$ over 32 fish) contributed to the data set, a concern is that the detected units are a result of false positives, arising from randomly fluctuating signals being classified purely by chance in one of the four functional categories. To address this, we applied a shuffle test, in which fluorescence traces were cut at 16 random time points and randomly rearranged, after which analysis proceeded as normal. The fact that the number of units in the four categories fell by a factor of 8.1 (Fig. 4h) indicates that the detected units did not arise by chance.

The motor-, gain increase-, gain decrease- and motor-off-based description of neural activity (Fig. 5a–d) is complementary to the CCFM- and CCFF-based description (Fig. 5e–f); the motor-based description derives from the gain-adaptation assay, and the CCFM- and CCFF-based description derives from the replay period, with both being useful functional descriptors of neural activity.

Lesions. Inferior olive lesions were performed by pre-selecting about 60 sites in an averaged two-photon image, then shining an infrared laser on them at 850 nm, at 900 mW power outside the cage. The pulses lasted 200 ms per site. During the exposure, the laser beam spiralled over a circle of 1 μm (ref. 24). Brief but large increases in emitted light intensity indicated a successful lesion; in the absence of such signals, the site was exposed once more, and abandoned if the second attempt failed.

50. Ruta, V., Datta, S. R., Vasconcelos, M. L., Freeland, J., Looger, L. L. & Axel, R. A dimorphic pheromone circuit in *Drosophila* from sensory input to descending output. *Nature* **468,** 686–690 (2010).
51. Hieber, V., Dai, X., Foreman, M. & Goldman, D. Induction of α1-tubulin gene expression during development and regeneration of the fish central nervous system. *J. Neurobiol.* **37,** 429–440 (1998).
52. Mukamel, E. A., Nimmerjahn, A. & Schnitzer, M. J. Automated analysis of cellular signals from large-scale calcium imaging data. *Neuron* **63,** 747–760 (2009).